

Engineering Higher Order Van Hove singularities in two dimensions: the example of the surface layer of Sr_2RuO_4

Anirudh Chandrasekaran,¹ Luke C. Rhodes,² Edgar Abarca Morales,^{2,3} Carolina A. Marques,^{2,*} Phil D.C. King,² Peter Wahl,^{2,4} and Joseph J. Betouras¹

¹*Department of Physics and Centre for the Science of Materials, Loughborough University, Loughborough LE11 3TU, United Kingdom*

²*SUPA, School of Physics and Astronomy, University of St Andrews, North Haugh, St Andrews, KY16 9SS, United Kingdom*

³*Max Planck Institute for Chemical Physics of Solids, Noethnitzer Strasse 40, 01187 Dresden, Germany*

⁴*Physikalisches Institut, Universität Bonn, Nussallee 12, 53115 Bonn, Germany*

(Dated: October 25, 2023)

The properties of correlated electron materials are often intricately linked to Van Hove singularities (VHs) in the vicinity of the Fermi energy. The class of these VHs is of great importance, with higher order ones – with power-law divergence in the density of states – leaving frequently distinct signatures in physical properties. We use a new theoretical method to detect and analyse higher order VHs (HOVHs) in two-dimensional materials and apply it to the electronic structure of the surface layer of Sr_2RuO_4 . We then constrain a low energy model of the VHs of the surface layer of Sr_2RuO_4 against angle-resolved photoemission spectroscopy and quasiparticle interference data to analyse the VHs near the Fermi level. We show how these VHs can be engineered into HOVHs.

Introduction. The properties of strongly correlated electron materials can be extremely sensitive to modest external stimuli, such as magnetic field, pressure or uniaxial strain, often exhibiting complex phase diagrams as a function of these tuning parameters [1–4]. In many cases, the sensitivity of their properties is traced back to van Hove singularities (VHs) in the vicinity of the Fermi energy (E_F) [5–8]. It has been realised that such VHs can also be of a higher-order type (HOVHs), where both the gradient and the Hessian determinant of the dispersion relation $\varepsilon(k_x, k_y)$ vanish and unique thermodynamic signatures can be observed [5, 9]. A detailed classification scheme of HOVHs is provided in Refs. [10]. Two of the authors have recently developed a new method to detect and analyse a HOVHs from arbitrary two dimensional electronic structure models [11, 12], enabling us to uniquely characterise the important band structure features in two dimensional systems.

Extending the method to real materials requires a detailed understanding of the material’s low-energy electronic structure. Here, we focus on the surface of Sr_2RuO_4 , which provides an ideal test system to explore how the symmetry and order of the VHs influences the electronic properties of multi-band and spin-orbit coupled (SOC) systems. Indeed, strontium ruthenates provide an ideal benchmark material class to explore the impact of VHs on macroscopic properties [1]. They host rich phase diagrams, with metamagnetic phases, a putative quantum critical point in $\text{Sr}_3\text{Ru}_2\text{O}_7$ [13] and evidence for unconventional superconductivity in Sr_2RuO_4 [14]. In both systems, there is strong evidence for the importance of VHs in their electronic properties [8, 15–19]. The superconductivity in Sr_2RuO_4 , for example, has been found to react sensitively to uniaxial strain [4] which directly

correlates with a VHs crossing E_F [8], while in $\text{Sr}_3\text{Ru}_2\text{O}_7$, an unusual field dependence of the specific heat has been explained from Zeeman splitting of HOVHs [5].

The surface layer of Sr_2RuO_4 provides a two-dimensional electronic system on which high-resolution spectroscopic data is available [17, 20–22], facilitating a full assessment of the nature of its VHs. A $\sqrt{2}\times\sqrt{2}$ structural reconstruction due to octahedral rotations [17, 20, 23, 24] results in a unit cell doubling that produces a four-fold saddle point in the electronic structure at the Brillouin zone (BZ) corner. This type of saddle point is an essential ingredient for the formation of a HOVHs (of classification type X_9 [10]) in $\text{Sr}_3\text{Ru}_2\text{O}_7$ [5] with power-law divergence in the density of states (DoS), distinct from the logarithmic divergence of the A_1 saddle point at the BZ face in the bulk of Sr_2RuO_4 .

In this work, we apply analytical and numerical tools to study how the octahedral rotation influences the formation of HOVHs in the surface layer of Sr_2RuO_4 . We first study the evolution of the VHs from density functional theory (DFT) calculations and establish the impact of octahedral rotations on the VHs, before constraining a minimal model directly against experimental data from angle-resolved photoemission spectroscopy (ARPES) and scanning tunnelling microscopy (STM). By combining these complementary data sets, we are able to progressively refine the low-energy electronic structure and obtain an accurate description of the dispersion relations in the vicinity of the saddle point. From the experimentally-derived model, we classify multiple VHs close to E_F and study how their order can be tuned, providing new design principles for VHs engineering in two-dimensional materials.

Octahedral rotation-induced order of VHs. To anal-

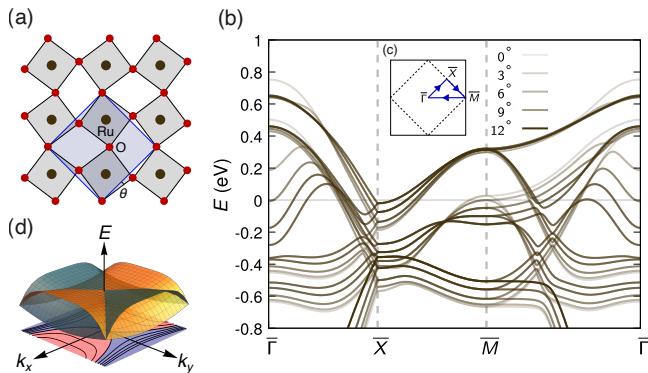


FIG. 1: **VHS in ruthenates.** (a) top-down view of a single layer of Sr₂RuO₄ highlighting the surface-induced octahedral rotation θ . Grey square shows the unit cell without octahedral rotations, the blue shaded square highlights the expanded unit cell with rotations. (b) Evolution of the band-structure as a function of θ . Darker lines correspond to larger Ru-O-Ru rotation angles. (c) BZ of Sr₂RuO₄ with octahedral rotations (dashed) and without (solid). (d) Fermi contours and 3D image of an A₃ HOVHs (and a $\pi/2$ rotated copy required by symmetry) that can occur at the M-point due to the reconstructed BZ.

use the impact of octahedral rotation on the electronic structure of Sr₂RuO₄, we perform DFT calculations of a monolayer of Sr₂RuO₄, shown in Fig. 1(a), with induced rotation of the RuO₆ octahedra, keeping the Ru-Ru distances constant. This produces a two-atom unit cell (Fig. 1(a)). We then calculate the electronic structure for each rotation angle and project onto a tight-binding model (TBM) [25]. There are two dominant changes as a function of octahedral rotation. First is the evolution of the saddle point VHS that lies close to E_F at the \bar{M} point. This band undergoes a Lifshitz transition at an octahedral rotation angle of $\sim 5^\circ$ and evolves from a concave dispersion to a convex dispersion as rotation angle increases. The second feature is the evolution and Lifshitz transition of an electron pocket at the $\bar{\Gamma}$ point. The energy of this band minimum is, however, known to be located too low in energy in DFT, with ARPES measurements placing it just above E_F [20, 24]. This only produces a linear offset to the DoS of the VHS around \bar{M} without affecting the order and symmetry of the relevant VHS around \bar{M} points. Here we focus only on the electronic structure of the low-energy VHS around the \bar{M} points [26].

Fig. 1(d) and Figs 2(a) and (b) show the electronic structure close the \bar{M} point and throughout the surface BZ, respectively, for a 9° octahedral rotation. The octahedral rotation significantly changes the curvature of the electronic structure from convex to concave in the vicinity of \bar{M} point. This continues tuning of the band dispersion leads to favorable conditions for the formation of HOVHs. By applying our method [11] to extract the

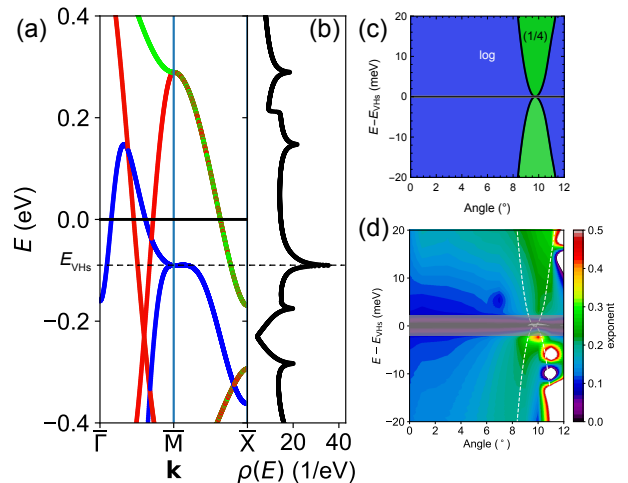


FIG. 2: (a) Band-structure in the vicinity of the M point showing the orbital character of VHS at a rotation angle $\theta = 9^\circ$. Colours encode orbital character (red: d_{xz} , green: d_{yz} , blue: d_{xy}). The energy E_{VHS} of the d_{xy} VHS is indicated by a horizontal dashed line. (b) DoS for the band structure shown in (a), with the VHS on the d_{xy} band. (c) Type of the d_{xy} VHS determined from the series expansion [10] as function of angle and energy from the VHS $E - E_{VHS}$. At an angle of $\theta \sim 9^\circ$, the behaviour exhibits a singular point at E_{VHS} where the VHS shows power-law divergence with exponent $-\frac{1}{4}$. (d) Numerically determined order of the tail of the VHS from $\frac{d \log \rho}{d \log E}$ for the d_{xy} -derived VHS as function of angle and energy. The energy scale is relative to the energy E_{VHS} at which the VHS occurs. The numerically determined order is not reliable in the grey area, because it is too close to the VHS. The dashed line shows the superimposed boundary between logarithmic and polynomial order of the tail of the VHS determined analytically.

order and symmetry of the VHS around the \bar{M} point, we find that close to $\theta \sim 9^\circ$, quadratic terms in the dispersion relation are suppressed in the $\bar{\Gamma} - \bar{M}$ direction and the analytic expansion predicts a HOVHs with an energy dependence in the tail of the DoS $\rho(E) \propto E^{-1/4}$, classified as A₃-type [10, 27]. For octahedral rotation angles below/above 9° , the dispersion is dominated by quadratic terms resulting in a VHS with a logarithmic divergence. Fig. 2(c) shows this phase diagram, as a function of energy and octahedral rotation angle.

The result demonstrates that modification of the octahedral rotation provides a method to engineer HOVHs in Sr₂RuO₄. However, in multi-band systems there is a possibility that other electronic states could mask the clean divergent signatures induced by HOVHs in thermodynamic properties. To check this possibility and establish the energy range over which the HOVHs impacts experimental observables, we numerically integrate the DoS $\rho(E)$ calculated using the TBM. The exponent of the VHS can then be determined from the logarithmic derivative of $\rho(E)$, $\frac{d \log \rho(E - E_{VHS})}{d \log E}$, which provides the order of

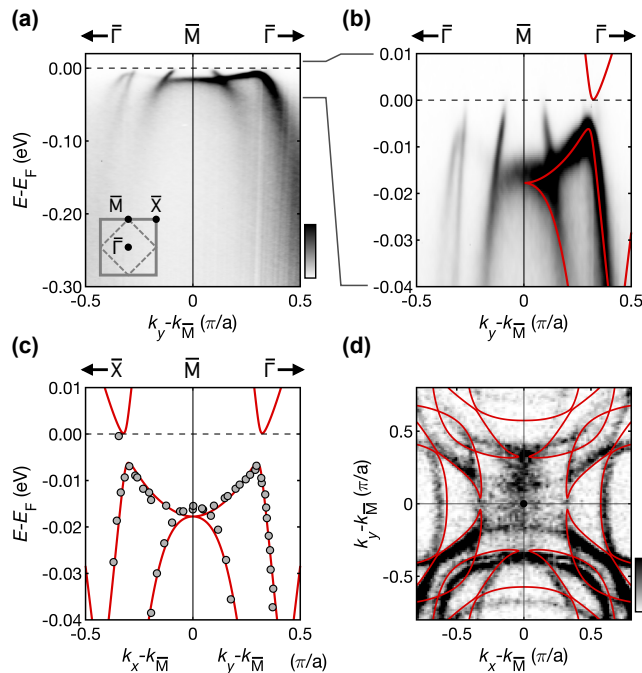


FIG. 3: **Electronic structure from ARPES and fitting of TBM.** (a) Band dispersions of the bulk and surface electronic structure of Sr₂RuO₄ measured by ARPES along the $\bar{\Gamma} - \bar{M}$ direction of the surface BZ, reproduced from Ref. [24]. (b) Zoom-in of the measured electronic structure near E_F , with the fitted TBM shown atop (red lines). The best-fit parameters are given in [28]. (c) The TBM is fitted to the bands extracted from the measurements shown in (b) and from additional measurements (Ref. [24]). (d) Corresponding Fermi surface measured by ARPES and calculated from our TBM.

the leading polynomial term in the tail of the VHs. The numerical analysis, shown in Fig. 2(d), confirms that the DoS tail from the VHs changes significantly as a function of rotation angle. While for small octahedral rotation angles we observe a behaviour consistent with a logarithmic divergence, as the angle θ approaches 9° , the VHs acquires an exponent $-1/4$, consistent with the analytic theory.

Fitting to ARPES. Having identified that HOVHs can be stabilised via octahedral rotations in monolayer Sr₂RuO₄, we turn our attention to a system that exhibits a series of VHs close to E_F with the potential to tune them, controlling their order. The surface of Sr₂RuO₄ is known to exhibit an octahedral rotation, with low energy electron diffraction measurements placing the angle at $\theta = 8.5 \pm 2.5^\circ$ [23], close to the critical angle of 9° at which the \bar{M} -point VHs becomes higher order. To establish the low energy model that describes the experimental electronic structure in the vicinity of the VHs at the \bar{M} point, we perform a polynomial interpolation of the DFT-derived TBMs as a function of angle and a least squares fitting to ARPES data of the surface electronic structure [24], presented in Fig. 3(a) [28]. We plot

the obtained TBM over the ARPES data in Fig. 3(b), and show this together with the extracted data points from the ARPES measurements used for the fitting in Fig. 3(c). The model shows excellent agreement with the ARPES data (Fig. 3(d)), and the octahedral rotation angle 8.03° is in agreement with measurements of the surface structure [23].

Comparison with QPI. The ARPES data reveal an important complication to the low-energy electronic structure of the surface of Sr₂RuO₄. Whilst they allowed us to locate the saddle point at around 18 meV below E_F , the bands in the vicinity of E_F are found to be dominated by a spin-orbit gap in the electronic structure which can also give rise to VHs in the DoS [24]. To gain further insight into the VHs mediated by this spin-orbit gap, we refine our experimental model of the VHs by comparing with QPI data obtained by STM at millikelvin temperatures and with sub-meV energy resolution. QPI provides access to the electronic states above and below E_F . Low-energy low-temperature differential conductance measurements of the surface of Sr₂RuO₄ were previously reported [17, 29] and established the existence of a partial gap with four peaks in the vicinity of E_F , indicating the presence of four close-lying VHs. However, when we compare a theoretical continuum LDoS calculation of the tunneling spectrum $g(V)$ from our ARPES-fit model to the STM measurements (shown in grey and black, respectively, in Fig. 4(a)), we find that although the model captures the partial gap, it only predicts two of the observed four peaks, and the position of the partial gap is several meV too low. The QPI data exhibits a small nematic term breaking the four-fold rotation symmetry of order ~ 1 meV [17, 29]. Incorporating this nematicity via an anisotropy of the nearest-neighbour hopping into our model, and adjusting the chemical potential by ~ 3 meV, we reproduce the experimental tunnelling conductance with sub-meV resolution. To confirm the accuracy of our model, we perform continuum QPI calculations, modelling scattering of electrons from a point-like defect, and compare with experimental data [29] (see supplementary for details). The calculation is in quantitative agreement with the experimental data within a ± 5 meV window. Fig. 4(b) shows a comparison between calculation and experiment of a representative constant energy cut, while Figs. 4(c,d) displays cuts as a function of energy.

We find that the formation of the gap-like structure close to the E_F can be understood completely as due to the near- E_F spin-orbit gap found in ARPES. By calculating the atomic corrugation of the real space LDOS using our new model, we find that SOC, coupled with a finite nematicity, produces the experimentally observed checkerboard modulation (Fig. 4(e,f)) [17], eliminating the need to introduce a checkerboard term into the TBM as suggested previously [17, 29]. Thus our model unifies ARPES and STM measurements of the low-energy elec-

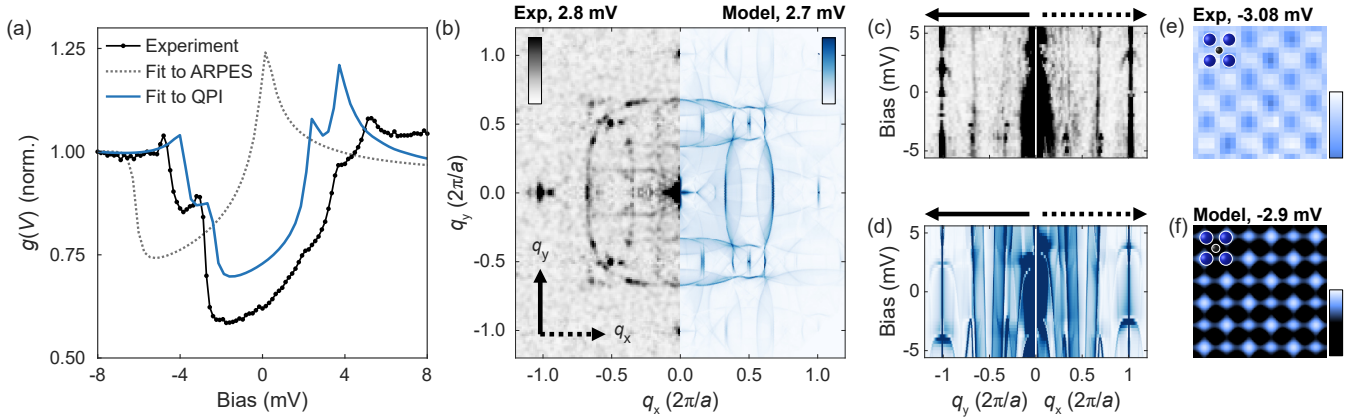


FIG. 4: **Low-energy electronic structure from QPI.** (a) Comparison of experimental and calculated tunneling spectrum of the clean surface, for the models fit to ARPES (grey, dotted) and to QPI (blue). (b) Left half: Quasi-particle interference image at $E = 2.8\text{mV}$, right half: calculations using model fitted to experimental data. (c-d) cuts through the atomic peaks along q_y (left) and q_x (right) from experiment (c) and calculations for the TBM fitted to the QPI (d). (e-f) Real-space image showing the checkerboard pattern at the Sr positions, from experiment (e) and the model (f). Blue and black spheres indicate the position of the Sr and Ru atoms, respectively.

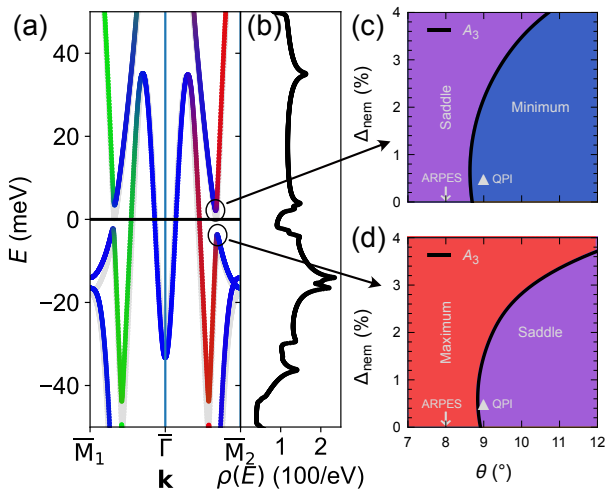


FIG. 5: **Analysis of spin-orbit induced VHS in the surface layer of Sr_2RuO_4 .** (a) Band structure and (b) DoS around E_F for the TBM fitted to QPI. Light grey lines in panel (a) show the band structure fitted to ARPES. (c, d) phase diagrams of the VHS closest to the E_F at the upper and lower edge of the SOC-induced gap, marked by circles in (a). Solid lines indicate the line where the VHS becomes an A_3 singularity. Similar results hold for the set of singularities close to \bar{M}_1 .

tronic structure of the surface of Sr_2RuO_4 with sub-meV energy resolution.

Order of the VHS. Our observation of a SOC-induced gap at E_F raises the question what the type of the VHS at the gap edge is. Fig. 5(a,b) presents the band structure, and corresponding DoS, of our final optimised TBM. This

model is quantitatively accurate around the \bar{M} point, now labelled by two subscripts due to the small nematic splitting rendering the M points inequivalent along the Ru-Ru reciprocal lattice directions.

We proceed to characterise the VHS found within 20 meV of E_F around the \bar{M} points taking into account the nematicity. The nematicity changes the critical angle where the HOVHS with the divergent exponent $-1/4$ (and class still A_3) is located. The critical line as a function of the percentage change of the nematicity, for values experimentally achievable through uniaxial strain, is computed (Fig. 5(c,d)). This line separates the regions of maximum/minimum and saddle point VHS, therefore the system can be tuned to an A_3 HOVHS by applying strain as a tuning parameter.

Discussion. In this work, we analyse two sets of complementary experimental data (STM and ARPES) of the benchmark material Sr_2RuO_4 . We are able to classify and understand the nature of HOVHS close to the Fermi surface. The work refines a long-standing question on the appearance of HOVHS in Sr_2RuO_4 , as evidenced through ARPES measurements very early [30, 31], before surface and bulk contributions were distinguished [20].

The combined theoretical and experimental characterization provides two key results: (i) the model for the low-energy electronic structure, consistent with STM and ARPES, captures related to the VHS. It provides an accurate description of the gap-like structure seen in tunneling spectra that were previously interpreted in terms of inelastic tunneling or correlation effects [22] or a hybridization gap [17, 32]. This gap can be explained straightforwardly as the combined result of SOC and octahedral rotation, leading to a suppression of DoS by almost 50%. Our low-energy model promises an under-

standing of the, yet unexplained, suppression of superconductivity in the surface layer of Sr_2RuO_4 [17, 33, 34]. (ii) From the series of TBMs used to fit the experimental data, we can deduce ‘design criteria’ for stabilizing HOVHs in Sr_2RuO_4 .

To this end, the introduced set of analytical and numerical tools enables the determination of the order of the HOVHs, leading to a phase diagram of their order. The d_{xy} -VHs clearly changes its type as a function of rotation angle, with a critical angle of $\sim 9.7^\circ$, surprisingly close to the angle realized in the surface reconstruction of Sr_2RuO_4 . Tunability of the rotation angle can be achieved by biaxial strain, as, for example, demonstrated in MBE-grown thin films [35]. In combination with doping or gating to control the chemical potential, thin films of strontium ruthenates become a promising testbed to establish the influence and importance of HOVHs for the physical properties. The theoretical and numerical tools we introduce here provide new methods to study tunable VHs in a range of existing quantum materials (e.g. [36]) and in many more predicted to exhibit almost flat bands [37]. Even weak interactions may lead to a plethora of quantum phases as a result of HOVHs [38, 39].

ACKNOWLEDGEMENTS

We thank Andy Mackenzie and Andreas Rost for useful discussions. We are grateful to the UK Engineering and Physical Sciences Research Council for funding via Grant Nos EP/T034351/1 and EP/T02108X/1. This work used computational resources of the Cirrus UK National Tier-2 HPC Service at EPCC (<http://www.cirrus.ac.uk>) funded by the University of Edinburgh and EPSRC (EP/P020267/1) and of the High-Performance Computing cluster Kennedy of the University of St Andrews.

SUPPLEMENTAL MATERIAL

Density Functional Theory Calculations

DFT calculations were performed using the augmented plane-wave code Quantum Espresso [40] using the PBE for the exchange-correlation functional. We used a monolayer of Sr_2RuO_4 with 15 Å of vacuum on either side for each calculation with the RuO_6 octahedra rigidly rotated by angles between 0 and 12° to study the role of octahedral rotation on the electronic structure. The energy cutoff for the wavefunction and charge density was chosen at 90 Ry and 720 Ry respectively and a \mathbf{k} -grid of $8 \times 8 \times 1$ was used for each calculation.

Tight-binding models (TBMs)

These DFT band structures were then projected onto an orthonormal tight binding basis consisting of the Ru d_{xz} , d_{yz} and d_{xy} orbitals in a two-atom unit cell. This was achieved using a modified version of Wannier90 [25] where we fix the phase of the Wannier functions against the first orbital to preserve the sign of the wave functions between neighbouring Ru atoms. This Wannierisation was performed on a $7 \times 7 \times 1$ \mathbf{k} -grid.

For fitting the ARPES band structure using the TBM, we perform a polynomial interpolation on the hopping strengths of the thirteen individual models obtained for angles $\theta = 0^\circ$ through 12° enabling fitting of θ as a continuous variable. We add a local spin orbit term $H_{\text{SOC}} = \lambda \mathbf{L} \cdot \mathbf{S}$. Lastly, we allow for an overall band renormalisation and shift of the chemical potential. Fitting the TBM to the ARPES band structure therefore implies optimizing the following free parameters: the SOC strength λ , RuO octahedral rotation angle θ , overall band renormalisation Z and the chemical potential μ .

For comparison with the QPI results, we introduce a nematicity of 0.5% across all orbitals, multiplying the nearest neighbour hoppings in one direction across all orbitals by 1.01 and dividing it in the orthogonal direction by 1.01.

Continuum Local DoS calculations

For continuum local DoS (LDoS) calculations shown in fig. 4, we use the TBM obtained from the fit to the ARPES data modified to be consistent with the STM differential conductance. We use the localized wave functions obtained at an angle close to the one obtained from the fit. Because the tunneling spectrum is significantly better described with a slightly larger octahedral rotation angle than the 8° obtained from the fit, we use as a basis the model and wave functions with $\theta = 9^\circ$. The continuum LDoS calculations are performed using the method introduced in [41–43] and recently applied to ruthenates [29, 44] using the St Andrews calcqpi code [19, 44–46]. Calculations shown in fig. 4 were done on a \mathbf{k} -space grid of 2048×2048 points distributed uniformly across the BZ of the two-atom unit cell. The real-space continuum LDoS is calculated over an area corresponding to 128×128 unit cells and with an energy broadening of 0.2 meV. We assume isotropic scattering with a scattering potential of $V = 1\text{eV}$ across all orbitals and spin directions.

Numerical Integration of DoS

We calculate the DoS $\rho(E)$ from the unperturbed Green’s function using $\rho(E) = -\text{Im}G_0(E)$ with an en-

ergy broadening of $\Gamma = 0.75\text{meV}$, and using a k -space grid with 2088×2088 over the first BZ. The DoS is calculated on a regular grid with an energy spacing of 0.4meV . To obtain the logarithmic derivative, we use a Savitzky-Golay algorithm with eleven points.

Tuning to a HOVHs

We briefly describe the procedure to tune the VHS in the TBMs into HOVHs. We first choose a band and a critical point of interest to us. Let us denote them by n and $\mathbf{k}^{(0)}$ respectively. If $\mathbf{k}^{(0)}$ is a critical point, then the gradient of the dispersion of band n vanishes, i.e. $\nabla \varepsilon_n(\mathbf{k}) = 0$ at $\mathbf{k} = \mathbf{k}^{(0)}$. If the Hessian determinant $\det[\partial_i \partial_j \varepsilon_n(\mathbf{k})]$ also vanishes at $\mathbf{k}^{(0)}$, we then have a HOVHs. Now the tight-binding Hamiltonian (and therefore the dispersion) also depend on the tuning parameters which we lump together as a vector \mathbf{t} . Therefore, the Hessian at any given \mathbf{k} is a function of \mathbf{t} as well. Thus, if we set the Hessian determinant evaluated at $\mathbf{k}^{(0)}$ to zero, we can solve for the critical value of \mathbf{t} that gives us a HOVHs at $\mathbf{k}^{(0)}$. To diagnose the type of the HOVHs, we will need the series expansion of the dispersion to a higher degree than just quadratic order (which is sufficient for computing the Hessian).

Now this procedure is fairly straightforward in theory: we simply have to analytically diagonalise the band Hamiltonian $H(\mathbf{k})$ and obtain the n^{th} band-dispersion as a function of \mathbf{k} , denoted by $\varepsilon_n(\mathbf{k})$. We can then calculate the partial derivatives of $\varepsilon_n(\mathbf{k})$ or equivalently compute its series expansion at the chosen $\mathbf{k}^{(0)}$ to any desired degree. However, it is usually possible to implement this analytic procedure only for two band Hamiltonians. Multi-band, detailed Hamiltonians necessitate the use of an alternate, computationally implementable strategy for obtaining the series expansion (and the partial derivatives).

The crux of this alternate method lies in the realisation that we only need to compute the *numerical* values of the partial derivatives $\partial^{l+m} \varepsilon_n(\mathbf{k}) / \partial^l k_x \partial^m k_y$ evaluated at $\mathbf{k}^{(0)}$ (for $1 \leq l+m \leq N$), in order to construct the Taylor expansion to degree N . In the one dimensional case, the first derivative can be computed using the Feynman - Hellmann lemma which reads

$$\left. \frac{d\varepsilon_n(k)}{dk} \right|_{k^{(0)}} = \left\langle n, k^{(0)} \left| \frac{dH(k)}{dk} \right|_{k^{(0)}} \right| n, k^{(0)} \rangle. \quad (1)$$

Note that this requires us to be able to 1) numerically obtain the eigenvector $|n, k^{(0)}\rangle$ and 2) differentiate the Hamiltonian matrix $H(\mathbf{k})$, both of which can be readily done, even in the case of large multi-band Hamiltonians. Therefore, to compute the full Taylor expansion in the two and three dimensional cases, we have to work with an appropriate generalisation of the Feynman - Hellmann

lemma which can also handle complicated multi-band degeneracies that often prop up at high-symmetry points. A comprehensive treatment of such an extension can be found in Ref [11]. The final formula for the Taylor expansion up to second order reads

$$\begin{aligned} \varepsilon_n(\mathbf{k}^{(0)} + \mathbf{k}) \approx & \left\langle n, \mathbf{k}^{(0)} \left| \frac{\partial H(\mathbf{k}^{(0)} + \lambda \mathbf{k})}{\partial \lambda} \right|_{\lambda=0} \right| n, \mathbf{k}^{(0)} \rangle \\ & + \left\langle n, \mathbf{k}^{(0)} \left| \frac{\partial^2 H(\mathbf{k}^{(0)} + \lambda \mathbf{k})}{\partial \lambda^2} \right|_{\lambda=0} \right| n, \mathbf{k}^{(0)} \rangle \\ & + \frac{1}{2} \sum_m \frac{\left| \left\langle n, \mathbf{k}^{(0)} \left| \frac{\partial H(\mathbf{k}^{(0)} + \lambda \mathbf{k})}{\partial \lambda} \right|_{\lambda=0} \right| m, \mathbf{k}^{(0)} \rangle \right|^2}{\varepsilon_n - \varepsilon_m} + \mathcal{O}(k^3), \end{aligned}$$

where $\mathbf{k} = (k_x, k_y)$ and the sum is over other the eigenvectors $|m, \mathbf{k}^{(0)}\rangle$ that are not degenerate to $|n, \mathbf{k}^{(0)}\rangle$. Note that only \mathbf{k} and λ are symbolic variables while $\mathbf{k}^{(0)}$, $|n, \mathbf{k}^{(0)}\rangle$ and $|m, \mathbf{k}^{(0)}\rangle$ are numerical vectors. This is what makes the method viable for large and complicated models. By using the auxiliary parameter λ in the formula above, we will directly obtain the series expansion as a multivariate polynomial in k_x and k_y . The partial derivatives can be extracted from the Taylor coefficients.

Furthermore, we can also readily track the effect of tuning parameters on the low-energy expansion by using $H(\mathbf{k}^{(0)} + \lambda \mathbf{k}, \mathbf{t}^{(0)} + \lambda \delta \mathbf{t})$ in place of $H(\mathbf{k}^{(0)} + \lambda \mathbf{k})$ in the formula above, where $\mathbf{t}^{(0)}$ is the set of tuning parameters (their chosen, numerical values to be precise). The perturbations to $\mathbf{t}^{(0)}$ will be incorporated through the symbolic vector $\delta \mathbf{t} = (\delta t_1, \delta t_2, \dots)$. In the present context, the tuning parameters of interest are the RuO octahedral rotation angle θ and the nematicity Δ_{nem} .

In this formulation, the numerical Taylor coefficients at the chosen $(\mathbf{k}^{(0)}, \theta^{(0)}, \Delta_{\text{nem}}^{(0)})$ will be perturbed by powers of $\delta \theta$, $\delta \Delta_{\text{nem}}$. We can then compute the Hessian determinant at $(\mathbf{k}^{(0)}, \theta^{(0)}, \Delta_{\text{nem}}^{(0)})$. This will be a polynomial in $\delta \theta$ and $\delta \Delta_{\text{nem}}$. We set it to zero to solve for $\delta \theta^*$ and $\delta \Delta_{\text{nem}}^*$. The critical values of the tuning parameters that yield a HOVHs are then given by $\theta^{(c)} \approx \theta^{(0)} + \delta \theta^*$ and $\Delta_{\text{nem}}^{(c)} \approx \Delta_{\text{nem}}^{(0)} + \delta \Delta_{\text{nem}}^*$. This process can be repeated a few times to obtain a more accurate value of the tuning parameters that lead to a HOVHs at $\mathbf{k}^{(0)}$.

The strategy outlined above works quite well at high-symmetry points like the \bar{M} wherein the location of the critical point remains fixed even as we change the tuning parameters. For the SOC gap VHS, we have to adopt a slightly different strategy. In this case, the location of the critical point $\mathbf{k}^{(0)}$ changes as we change θ and Δ_{nem} . For Δ_{nem} in the range of 0% to 4%, we find that the Hessian determinant for the critical points in the SOC gap changes sign in the range of 8° to 12° . So for any given Δ_{nem} , we perform binary search to find the value of θ at which the Hessian determinant vanishes. At any intermediate θ , we have to compute the new location of $\mathbf{k}^{(0)}$. We start at an approximate location and Taylor

expand the band to cubic or quartic order. This gives a polynomial approximation for $\varepsilon_n(\mathbf{k})$ near $\mathbf{k}^{(0)}$. We can compute the gradient of this, set it to zero and solve the resultant system of simultaneous polynomial equations numerically. Choosing the smallest real solution, we can arrive at a more accurate estimate for $\mathbf{k}^{(0)}$. We repeat this a few times to attain convergence and proceed with computing the Hessian determinant at $\mathbf{k}^{(0)}$.

* present address: Physik-Institut, Universität Zürich, Winterthurerstrasse 190, CH-8057 Zürich, Switzerland

- [1] B. Binz and M. Sigrist, EPL (Europhysics Letters) **65**, 816 (2004).
- [2] A. Hackl and M. Vojta, Physical Review Letters **106**, 137002 (2011).
- [3] A. Shtyk, G. Goldstein, and C. Chamon, Phys. Rev. B **95**, 035137 (2017), ISSN 2469-9950, 2469-9969, URL <https://link.aps.org/doi/10.1103/PhysRevB.95.035137>.
- [4] A. Steppke, L. Zhao, M. E. Barber, T. Scaffidi, F. Jerzembeck, H. Rosner, A. S. Gibbs, Y. Maeno, S. H. Simon, A. P. Mackenzie, et al., Science **355**, eaaf9398 (2017).
- [5] D. V. Efremov, A. Shtyk, A. W. Rost, C. Chamon, A. P. Mackenzie, and J. J. Betouras, Physical Review Letters **123**, 207202 (2019).
- [6] Y. Sherkunov and J. J. Betouras, Phys. Rev. B **98**, 205151 (2018).
- [7] N. F. Q. Yuan, H. Isobe, and L. Fu, Nat Commun **10**, 5769 (2019), ISSN 2041-1723, URL <http://www.nature.com/articles/s41467-019-13670-9>.
- [8] V. Sunko, E. A. Morales, I. Marković, M. E. Barber, D. Milosavljević, F. Mazzola, D. A. Sokolov, N. Kikugawa, C. Cacho, P. Dudin, et al., npj Quantum Materials **4**, 46 (2019).
- [9] A. Chandrasekaran and J. J. Betouras, Phys. Rev. B **105**, 075144 (2022).
- [10] A. Chandrasekaran, A. Shtyk, J. J. Betouras, and C. Chamon, Phys. Rev. Research **2**, 013355 (2020), ISSN 2643-1564, URL <https://link.aps.org/doi/10.1103/PhysRevResearch.2.013355>.
- [11] A. Chandrasekaran and J. J. Betouras, Advanced Physics Research **2**, 2200061 (2023), ISSN 2751-1200, 2751-1200, URL <https://onlinelibrary.wiley.com/doi/10.1002/apxr.202200061>.
- [12] The method expands the dispersion relation directly in the vicinity of the VHs, and utilises the Feynmann-Hellmann theorem to evaluate higher-order derivatives.
- [13] S. Grigera, R. Perry, A. Schofield, M. Chiao, S. Julian, G. Lonzarich, S. Ikeda, Y. Maeno, A. Millis, and A. Mackenzie, Science **294**, 329 (2001).
- [14] Y. Maeno, H. Hashimoto, K. Yoshida, S. Nishizaki, T. Fujita, J. G. Bednorz, and F. Lichtenberg, Nature **372**, 532 (1994).
- [15] M. P. Allan, A. Tamai, E. Rozbicki, M. H. Fischer, J. Voss, P. D. C. King, W. Meevasana, S. Thirupathiah, E. Rienks, J. Fink, et al., New Journal of Physics **15**, 063029 (2013), URL <https://dx.doi.org/10.1088/1367-2630/15/6/063029>.
- [16] K. M. Shen, N. Kikugawa, C. Bergemann, L. Balicas, F. Baumberger, W. Meevasana, N. J. C. Ingle, Y. Maeno, Z.-X. Shen, and A. P. Mackenzie, Phys. Rev. Lett. **99**, 187001 (2007), URL <https://link.aps.org/doi/10.1103/PhysRevLett.99.187001>.
- [17] C. A. Marques, L. C. Rhodes, R. Fittipaldi, V. Granata, C.-M. Yim, R. Buzio, A. Gerbi, A. Vecchione, A. W. Rost, and P. Wahl, Advanced Materials **33**, 2100593 (2021).
- [18] C. A. Marques, L. C. Rhodes, I. Benedičič, M. Naritsuka, A. B. Naden, Z. Li, A. C. Komarek, A. P. Mackenzie, and P. Wahl, Sci. Adv. **8**, eabo7757 (2022), URL <https://www.science.org/doi/10.1126/sciadv.abo7757>.
- [19] C. A. Marques, P. A. E. Murgatroyd, R. Fittipaldi, W. Osmolska, B. Edwards, I. Benedičič, G.-R. Siemann, L. C. Rhodes, S. Buchberger, M. Naritsuka, et al., *Spin-orbit coupling induced Van Hove singularity in proximity to a Lifshitz transition in Sr₄Ru₃O₁₀* (2023), arXiv:2303.05587 [cond-mat], URL <http://arxiv.org/abs/2303.05587>.
- [20] A. Damascelli, D. H. Lu, K. M. Shen, N. P. Armitage, F. Ronning, D. L. Feng, C. Kim, Z.-X. Shen, T. Kimura, Y. Tokura, et al., Phys. Rev. Lett. **85**, 5194 (2000), URL <https://link.aps.org/doi/10.1103/PhysRevLett.85.5194>.
- [21] A. Tamai, M. Zingl, E. Rozbicki, E. Cappelli, S. Riccò, A. de la Torre, S. McKeown Walker, F. Y. Bruno, P. D. C. King, W. Meevasana, et al., Phys. Rev. X **9**, 021048 (2019), URL <https://link.aps.org/doi/10.1103/PhysRevX.9.021048>.
- [22] Z. Wang, D. Walkup, P. Derry, T. Scaffidi, M. Rak, S. Vig, A. Kogar, I. Zeljkovic, A. Husain, L. H. Santos, et al., Nature Physics **13**, 799 (2017), ISSN 1745-2473, 1745-2481, URL <http://www.nature.com/articles/nphys4107>.
- [23] R. Matzdorf, Ismail, T. Kimura, Y. Tokura, and E. W. Plummer, Phys. Rev. B **65**, 085404 (2002), URL <https://link.aps.org/doi/10.1103/PhysRevB.65.085404>.
- [24] E. A. Morales, G.-R. Siemann, A. Zivanovic, P. A. E. Murgatroyd, I. Markovi, B. Edwards, C. A. Hooley, D. A. Sokolov, N. Kikugawa, C. Cacho, et al., Physical Review Letters **130**, 096401 (2023), URL <https://journals.aps.org/prl/abstract/10.1103/PhysRevLett.130.096401>.
- [25] G. Pizzi, V. Vitale, R. Arita, S. Blügel, F. Freimuth, G. Géranton, M. Gibertini, D. Gresch, C. Johnson, T. Koretsune, et al., Journal of Physics: Condensed Matter **32**, 165902 (2020), URL <https://doi.org/10.1088/1361-648x/ab51ff>.
- [26] Known mechanisms to remove this pocket would require e.g DFT + U, or modification of the energies of the e_g bands, neglected in these models.
- [27] N. F. Q. Yuan and L. Fu, Phys. Rev. B **101**, 125120 (2020), URL <https://link.aps.org/doi/10.1103/PhysRevB.101.125120>.
- [28] Specifically, we perform a grid-based search in a parameter space that includes octahedral rotation, θ , SOC λ , and a quasiparticle renormalisation factor, Z [47]. The best fit to the ARPES bands in the vicinity of the \bar{M} point are $\theta = 8.03^\circ$, $\lambda = 0.17$ eV, and $Z = 0.24$. For more details see Supplemental Material.
- [29] A. Kreisel, C. A. Marques, L. C. Rhodes, X. Kong, T. Berlijn, R. Fittipaldi, V. Granata, A. Vecchione, P. Wahl, and P. J. Hirschfeld, npj Quantum Mater. **6**,

- 100 (2021), ISSN 2397-4648, URL <https://www.nature.com/articles/s41535-021-00401-x>.
- [30] D. H. Lu, M. Schmidt, T. R. Cummins, S. Schuppler, F. Lichtenberg, and J. G. Bednorz, *Phys. Rev. Lett.* **76**, 4845 (1996).
- [31] T. Yokoya, A. Chainani, T. Takahashi, H. Katayama-Yoshida, M. Kasai, and Y. Tokura, *Phys. Rev. Lett.* **76**, 3009 (1996).
- [32] A. Kreisel, C. Marques, L. Rhodes, X. Kong, T. Berlijn, R. Fittipaldi, V. Granata, A. Vecchione, P. Wahl, and P. Hirschfeld, *npj Quantum Materials* **6**, 100 (2021).
- [33] B. Barker, S. Dutta, C. Lupien, P. McEuen, N. Kikugawa, Y. Maeno, and J. Davis, *Physica B: Condensed Matter* **329-333**, 1334 (2003), ISSN 09214526, URL <http://linkinghub.elsevier.com/retrieve/pii/S0921452602021580>.
- [34] H. Kambara, Y. Niimi, K. Takizawa, H. Yaguchi, Y. Maeno, and H. Fukuyama, in *AIP Conference Proceedings* (AIP, Orlando, Florida (USA), 2006), vol. 850, pp. 539–540, URL <http://aip.scitation.org/doi/abs/10.1063/1.2354823>.
- [35] B. Burganov, C. Adamo, A. Mulder, M. Uchida, P. D. C. King, J. W. Harter, D. E. Shai, A. S. Gibbs, A. P. Mackenzie, R. Uecker, et al., *Phys. Rev. Lett.* **116**, 197003 (2016), URL <http://journals.aps.org/prl/abstract/10.1103/PhysRevLett.116.197003>.
- [36] B. Liu, M.-Q. Kuang, Y. Luo, Y. Li, C. Hu, J. Liu, Q. Xiao, X. Zheng, L. Huai, S. Peng, et al., *Phys. Rev. Lett.* **131**, 026701 (2023).
- [37] N. Regnault, Y. Xu, M.-R. Li, D.-S. Ma, M. Jovanovic, A. Yazdani, S. S. P. Parkin, C. Felser, L. M. Schoop, N. P. Ong, et al., *Nature* **603**, 824 (2022).
- [38] A. Zervou, D. V. Efremov, and J. J. Betouras, *Phys. Rev. Res.* **5**, L042006 (2023), URL <https://journals.aps.org/prresearch/pdf/10.1103/PhysRevResearch.5.L042006>.
- [39] L. Classen, A. V. Chubukov, C. Honerkamp, and M. M. Scherer, *Phys. Rev. B* **102**, 125141 (2020).
- [40] P. Giannozzi, O. Andreussi, T. Brumme, O. Bunau, M. B. Nardelli, M. Calandra, R. Car, C. Cavazzoni, D. Ceresoli, M. Cococcioni, et al., *Journal of Physics: Condensed Matter* **29**, 465901 (2017), URL <https://doi.org/10.1088/1361-648x/aa8f79>.
- [41] P. Choubey, T. Berlijn, A. Kreisel, C. Cao, and P. Hirschfeld, *Phys. Rev. B* **90**, 134520 (2014), URL <http://link.aps.org/doi/10.1103/PhysRevB.90.134520>.
- [42] A. Kreisel, P. Choubey, T. Berlijn, W. Ku, B. Andersen, and P. Hirschfeld, *Phys. Rev. Lett.* **114**, 217002 (2015), URL <https://link.aps.org/doi/10.1103/PhysRevLett.114.217002>.
- [43] P. Choubey, A. Kreisel, T. Berlijn, B. M. Andersen, and P. J. Hirschfeld, *Phys. Rev. B* **96**, 174523 (2017), ISSN 2469-9950, 2469-9969, URL <https://link.aps.org/doi/10.1103/PhysRevB.96.174523>.
- [44] I. Benedičič, M. Naritsuka, L. C. Rhodes, C. Trainer, Y. Nanao, A. B. Naden, R. Fittipaldi, V. Granata, M. Lettieri, A. Vecchione, et al., *Physical Review B* **106**, L241107 (2022), URL <https://journals.aps.org/prb/abstract/10.1103/PhysRevB.106.L241107>.
- [45] L. C. Rhodes, W. Osmolska, C. A. Marques, and P. Wahl, *Phys. Rev. B* **107**, 045107 (2023), ISSN 2469-9950, 2469-9969, URL <https://link.aps.org/doi/10.1103/PhysRevB.107.045107>.
- [46] M. Naritsuka, I. Benedičič, L. C. Rhodes, C. A. Marques, C. Trainer, Z. Li, A. C. Komarek, and P. Wahl, *Proceedings of the National Academy of Sciences* **120**, e2308972120 (2023).
- [47] Details can be found in the Supplemental material.